Nanoscale

PAPER

View Article Online
View Journal | View Issue



Cite this: *Nanoscale*, 2025, **17**, 16837

# van der Waals pressure assisted synthesis of solid state nanomercury from mercury salts under ambient conditions: a sustainable approach for effortless Hg(II) removal from wastewater and safe storage thereof†

T. P. Amrutha,[a] Vakayil K. Praveen [b,c] and Renuka Neeroli Kizhakayil *[a]

The synthesis and characterisation of stable solid mercury nanoparticles (HgNPs) face significant hurdles, as the physical properties of the material under ambient conditions limit the fabrication and characterisation of the element in the nanoregime. Extremely stringent conditions (1.2 GPa or −38 °C) are mandatory for achieving mercury in the solid state. Here crystalline mercury stabilized in turbostratic nitrogen-doped graphenic matrix (t-NG) is achieved from aqueous $Hg^{2+}$ at room temperature, using a simple procedure involving N-doped graphene oxide quantum dots (NGOQDs). Solid crystalline nanomercury formation in graphenic layers is verified by transmission electron microscopy (TEM), atomic force microscopy (AFM), X-ray diffraction (XRD) and X-ray photoelectron spectroscopy (XPS), which is further backed by Raman spectral analysis. The solid mercury lattice exhibited rhombohedral α-phase and showed considerable crystallinity at room temperature. Excellent stability of the HgNPs lasting for months under ambient laboratory conditions warrants the scope of the system for further applications. Furthermore, the strategy furnishes a novel and efficient method for the detection and removal of the highly soluble mercury ions Hg(II) from waste water using NGOQDs. The method also offers a provision for safe storage of the species in the solid state, thus claiming advantage over traditional adsorptive removal methods, where the management of adsorbed ions remains a hurdle.

Received 13th March 2025,
Accepted 2nd June 2025

DOI: 10.1039/d5nr01066g

rsc.li/nanoscale



## 1. Introduction

van der Waals forces existing between 2D structures have been a hot topic of discussion recently, due to the scope of designing novel materials with tailored properties.[1,2] When nanoenclosures are created in interlayer spaces of these 2D materials at room temperature, high pressure is built up within these confined spaces, which is extremely high in the sub-nanometre regime.[1] These forces are expected to generate unusual properties in molecules/species enclosed in interlayers of such materials. Graphene falls in the category of such 2D materials, where the above-mentioned nanoconfined spaces are utilised for various technical applications.[3,4] Herein, we report the utilisation of van der Waals pressure operating in graphenic layers for the room temperature synthesis of solid state mercury, Hg(0), which otherwise exists in the liquid phase under ambient conditions. Mercury, featuring atypical physicochemical characteristics, claims numerous unique and advantageous aspects as well as a dark side, where the element is utmost fatal to mankind and the environment.[5] The physical properties of this element under ambient conditions hamper the fabrication and characterization of the element in the nanoregime, making it one of the least explored members among the metal nanoparticles. Only a few studies are available that showcase the synthesis of nanoscale mercury, as detailed below. Colloids formed *via* ultrasonic dispersion[6] and chemical reduction[7,8] have shown UV-visible absorption peak corresponding to nanomercury,[9] though a stable solid state was not identified. Majumder and co-workers have identified cubic mercury nanoparticles embedded in a plasmid DNA scaffold.[10,11] Attempts have also been made to trap liquid mercury nanodrops by embedding the nanoparticles in

[a]*Advanced Materials Research Centre, Department of Chemistry, University of Calicut, Kerala 673635, India. E-mail: renuka@uoc.ac.in*
[b]*Photosciences and Photonics Section, Chemical Sciences and Technology Division, CSIR-National Institute for Interdisciplinary Science and Technology (CSIR-NIIST), Thiruvananthapuram, Kerala 695019, India*
[c]*Academy of Scientific and Innovative Research (AcSIR), Ghaziabad 201002, India*

† Electronic supplementary information (ESI) available: The experimental details of the synthesis and characterisation of NGOQDs and stabilised nanomercury. See DOI: https://doi.org/10.1039/d5nr01066g

suitable matrices. In this line, polymer matrix entrapped liquid mercury nanodrops were attained under normal conditions.[12] Apart from this, carbon shell encapsulated nanodrops of liquid mercury were achieved by the thermolysis of dimethyl mercury, using RAPET (reaction under autogenic pressure at elevated temperatures) synthesis.[13]

Realization of solid state nanomercury is even harder, and requires extremely harsh conditions. Mercury can exist in four solid phases, namely, α, β, γ and δ. The least harsh conditions requirement is for the α phase with a rhombohedral structure, and is obtained either by pressurizing liquid mercury above 1.2 GPa at room temperature or by cooling it below 234 K at atmospheric pressure. Further higher pressures/lower temperatures are mandatory for achieving other solid phases.[14] At this context, it is noteworthy that Ramesh *et al.* could achieve polymer matrix entrapped solid state mercury when the temperature was lowered to −120 °C.[12] The liquid–solid phase transition of the element has been an interesting topic of study for researchers. The effect of restricted geometry of the host matrix on the melting–crystallization phase transition of mercury was revealed by investigating mercury confined in nanospaces. In this line, NMR signals corresponding to solid mercury were identified in the nanopores of activated carbon and silica gel at temperatures below 230 and 225 K, respectively.[15] Borisov and co-workers have probed the role of pore geometry of the matrices in favoring the solidification of the element using porous glass.[16,17] However, in this case, solidification was noted only at temperatures far below the ambient conditions. To the best of our knowledge, only two reports are available on the synthesis and characterization of stable solid crystalline nanoform of mercury to date. It is worth mentioning that this is achieved on layered 2D lattices, which stabilize the nanoparticles in the solid rhombohedral α-form of the element.[18,19] In the first report, Harika *et al.* achieved reduced graphene oxide (rGO) stabilized solid HgNPs from liquid metallic mercury through a sonochemical route.[18] The high acoustic pressure during the propagation of ultrasonic waves provides a suitable environment for the solidification of liquid mercury (1.2 GPa).[20,21] The stability of HgNPs on rGO was attributed to the electronic interactions with slight charge transfer that exists between the mercury (donor) and the oxygen functionalities of rGO (acceptor), irrespective of the size of the nanoparticle.[18] Eventually, this is based on the role of graphene to perform as an excellent substrate by serving as nucleation sites and dispersion centers for metal nanoparticles, thus reducing aggregation, keeping the innate properties of the latter intact.[22,23] To be specific, the oxygen functionalities/structural defects on rGO serve as active centers here.[24–26] In the second report, Kana *et al.* have shown solid state HgNPs of size 2.4 nm, trapped in a turbostratic boron nitride (BN) matrix.[19] However, the poorly developed solid rhombohedral α-phase exhibited Braggs diffraction peaks corresponding to only (101) and (003) planes. Well-defined peaks characteristic of the rhombohedral form are identified only at liquid nitrogen temperature. Apart from the atomic scale ordering in ultra-small HgNPs, the stability of the solid state is attributed to the low compressibility of the host matrix of high mechanical strength and the turbostratic structural form. An apparent crystalline nature is observed only with the concomitant evolution of discernible peaks of turbostratic BN, which hints at the decisive role of misaligned matrices in preventing the coalescence of individual particles through appropriate trapping.[19] Such detention of HgNPs in interlayer spaces of rGO sheets is observed in the report of Harika *et al.* also.[18]

Herein, we show solid state lattice formation of mercury atoms when confined/intercalated in interlayers of a turbostratic nitrogen-doped graphene (t-NG) matrix under ambient conditions. The synthesis route involves the conventional reduction strategy in which the mercury ions are coverted to Hg(0) by nitrogen doped GOQDs. Metal ion induced self-assembly of NGOQDs weaves up the t-NG matrix, through the concomitant involvement of pH[27,28] and the oxygen functional groups,[29] and effectively confines Hg(0) in the 2D solid lattice. The harsh conditions mandatory for mercury solidification at room temperature (1.2 GPa pressure) are realised through the intercalation of the HgNPs in the graphene layers, which exerts sufficient van der Waals pressure to keep the element in the solid state.[1,2,30] The solid crystalline nature and the stability of mercury nanoparticles are confirmed through TEM, AFM, XRD analyses, energy dispersive X-ray (EDX) analysis, XPS, and Raman spectroscopy techniques. The crystallinity of the solid HgNPs was significantly higher than that in the reports mentioned earlier.[18,19] The highlight of the report is the effortless synthesis strategy involved in attaining nanomercury crystals under ambient conditions from mercury salts. This study underlines the advantage of van der Waals pressure developed in layered lattices of high mechanical strength for achieving materials with distinct features, which are otherwise feasible only under stringent environments.

The result further furnishes an efficient method of detection and removal of the highly soluble toxic mercury ions Hg(II) from waste water using NGOQDs, as mere treatment of the former with NGOQDs leads to solid residue (nanomercury trapped in graphenic matrix) which can be filtered off effortlessly upon centrifugation. The method also offers a provision of storing the species in the solid state, and claims advantage over traditional adsorptive removal of analyte ions, where the management of adsorbed ions still remains a hurdle.

## 2. Results and discussion

### 2.1. Characterisation of NGOQDs

The experimental details on the synthesis and characterisation of NGOQDs and the stabilised nanomercury are provided in the ESI (sections 1 and 2).† Hydrothermal treatment of *ortho*-phenylenediamine yielded a yellowish solution of carbon particles (NGOQDs) that show yellow luminescence under UV illumination (Fig. 1a). The morphology and size of the NGOQDs were analyzed using TEM images (Fig. 1b–d). The TEM image provided in Fig. 1b validates the spherical morphology of par-

 

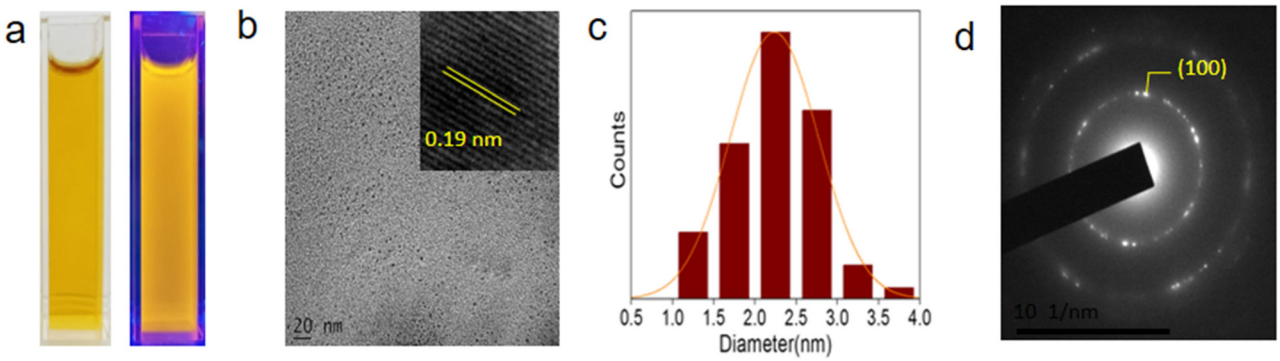


**Fig. 1** Physical characteristics of NGOQDs. (a) Photographs of NGOQD aqueous dispersions under day light and 365 nm UV light, (b) HR-TEM image of NGOQDs; the inset shows lattice fringes, (c) size distribution histogram of NGOQDs obtained from the TEM image, and (d) SAED pattern of NGOQDs.



ticles. Lattice fringes with a *d*-spacing value of 0.19 nm are discernible in the high-resolution TEM image given in the inset. An average particle size of 2.2 nm is evident from the particle distribution histogram provided in Fig. 1c and the polycrystalline nature of the system is shown by the SAED pattern in Fig. 1d. The XRD study provides additional evidence for the crystalline nature of the sample (Fig. S1a, ESI†). The most intense peak is noted at a $2\theta$ value of 8.5°, signifying the (001) lattice plane, corresponding to the *d*-spacing value of 1.03 nm, while the second peak is observed at 17.5°, which corresponds to 0.51 nm, representing the (002) plane.[31,32] Both the peaks indicate a highly oxygen functionalized basal plane in the carbon framework, analogous to a graphene oxide structure. One more peak is observed in the XRD pattern of NGOQDs at 44.4° with a *d*-spacing value of ~0.2 nm corresponding to the (100) lattice plane of carbon (JCPDS File 41-1487). The *d*-spacing value calculated from the SAED pattern matches well with the interplanar distance of the (100) plane obtained from the XRD of the system (Fig. S1a, ESI†).

The distinct wide band between 3100 and 3800 $cm^{-1}$ observed in the FTIR spectrum of NGOQDs (Fig. S1b, ESI†) shows the presence of hydroxyl functionalities in the carbon matrix. The presence of C≡N group is indicated by the band noted at 2339 $cm^{-1}$.[33] The weak stretching vibration of C≡C is envisaged by the broad absorption band centered at 2084 $cm^{-1}$.[34] This type of bonding is reported when the graphene sheet is cut along an armchair line.[35] The band located at around 1636 $cm^{-1}$ is associated with the C=C vibrations present in the aromatic carbon framework. Vibrations of various other functional groups contribute within this range. These include the C=O vibrations of imide bands, non-aromatic double bonds, the C=O group in ketones and quinones involved in H-bonds, and the symmetrical stretching of the $COO^-$ group. The band observed at 1439 $cm^{-1}$ can be ascribed to symmetrical deformations of $CH_3$ and the in-plane deformation of O–H, while the one at 600 $cm^{-1}$ results from angular deformations outside the C–H aromatic rings.[34] The peak observed at 1032 $cm^{-1}$ is assigned to the C–O vibration within C–O–C groups.[36] The peak observed at 1383 $cm^{-1}$ signifies the stretching modes of C=N/C–N bonds.[37]

Further proof for the nature of the carbon core and functional groups is provided by the XPS results (Fig. S1c and Fig. S2a–c, ESI†) of NGOQDs. Three peaks at 300.8, 414.1 and 547.3 eV seen in the XPS survey spectrum of the system (Fig. S1c, ESI†) are assigned to the C 1s, N 1s, and O 1s signals, respectively. Relative molar concentrations of 79.24, 12.57, and 8.19%, respectively are indicated for the C, N, and O elements, from the binding energy values and relative areas under the peaks. The C 1s spectrum (Fig. S2a, ESI†) shows five distinct peaks at 283.8 eV for C≡C,[38] 284.7 eV signifying C=C/C–C groups, 285.5 eV indicating the C–N bond, 286 eV originating from the –C–O bond, and 287.3 eV characteristic of the –C=O bond.[39] The N 1s spectrum (Fig. S2b, ESI†) reveals two distinct peaks at 396.6 eV (pyridinic Ns) and 397.9 eV (pyrrolic N).[40] The O 1s spectrum (Fig. S2c, ESI†) is fitted with two peaks, at 529.8 and 531.5 eV, that correspond to –C=O and C–OH/C–O–C moieties, respectively.[41]

Fig. S1d, ESI† shows the Raman spectrum of the NGOQDs, offering insights into the conjugated and carbon–carbon double bonds that result in intense peaks in the Raman spectrum. Specifically, the G band is situated at 1516 $cm^{-1}$, corresponding to the $E_{2g}$ phonon of $sp^2$ carbon atoms, while the D band is positioned at 1391 $cm^{-1}$, which signifies the breathing mode of *k*-point phonons with $A_{1g}$ symmetry. The D and G bands are attributed, respectively to vibrations in $sp^3$ and $sp^2$ carbon atoms. The G band is linked to the vibration of $sp^2$ carbon atoms within the graphitic lattice. The D band signifies disorder, which could stem from defects like vacancies, grain boundaries, and amorphous carbon species. The ratio of intensities between these two bands, $I_D/I_G$, holds the key for predicting the defects in the carbon lattice. In this case, the band intensity ratio is 0.80, decisively indicating the prevalence of $sp^2$ carbon domains in contrast to $sp^3$ carbon structures.[42,43] An additional peak at 1239 $cm^{-1}$ is also evident, denoted as D*, which emerges from the vibrations of carbon atoms constrained by oxygen-containing groups.[44]

Fig. S3a, ESI† shows the UV-vis absorption spectrum of the NGOQD system. The peaks at 205 and 235 nm signify the π–π* transitions of aromatic C=C bonds, whereas the peak at 288 nm is attributed to n–π* transitions of C=O groups.[45,46] The broad absorption observed at around 413 nm is attributed to the n–π* transition of C=O bonds, and it also indicates the presence of amine groups. Thus distinct absorption states arise from variations in the π-conjugated electron system.[47,48] Furthermore, this observation serves as an additional confirmation for the existence of oxygenated groups within the NGOQDs. The excitation ($\lambda_{max}$ = 370 nm) and emission spectra ($\lambda_{max}$ = 562 nm) of NGOQDs are shown in Fig. S3b, ESI.† A thorough fluorescence emission spectral examination using several excitation wavelengths is shown in Fig. S3c, ESI.† It is noted that the fluorescence emission peak at 562 nm does not change when the excitation wavelength is increased from 370 to 420 nm. The excitation-independent emission behaviour is thought to be connected with smaller surface flaws and size uniformity of the particlces.[41] These observations are consistent with the TEM results. The fluorescence lifetime of NGOQDs at room temperature is evaluated using the TCSPC method. The average lifetime ($\tau_{av}$) is noted as 2.35 ns (Fig. S3d, ESI†). Considerable photostability is also attributed to the system (Fig. S3e, ESI†), where the emission intensity showed only a marginal change even after continuous UV irradiation for 3 h.

### 2.2. Interaction of NGOQDs with mercury ions

An interesting observation was made from the interaction of $Hg^{2+}$ ions with NGOQDs. A visible change was observed in the NGOQD solution after adding the Hg(II) solution. An initial turbidity was noted within minutes, which ended up in precipitate formation that settled down within ~20 min (Fig. 2a). The solid and liquid fractions were collected separately and analysed further. The solid material, supposed to be a NGOQD–Hg mixture, was subjected to detailed analysis using XRD, TEM, EDX, XPS, FT-IR spectral analysis, Raman spectral analysis, and AFM study. XRD analysis of the solid revealed the crystalline nature of the system. Major peaks are noted at 21.3, 28, 32.8, 40.3, 43.7, 46.3, 52.7, 63.1, 68.3, and 76.2° (Fig. 2b). Among these, a striking feature was the absence of peaks at 8.5 and 17.5°, when the peaks characteristic of the carbon material are analysed, in comparison with the starting NGOQD system. At the same time, additional peaks are observed at 22, 28, 43.1 and 46.3°. The absence of the first two peaks indicates that the interplanar distance between the basal planes of carbon frameworks is now reduced, presumably due to the lesser number of functional groups involved. Changes in the

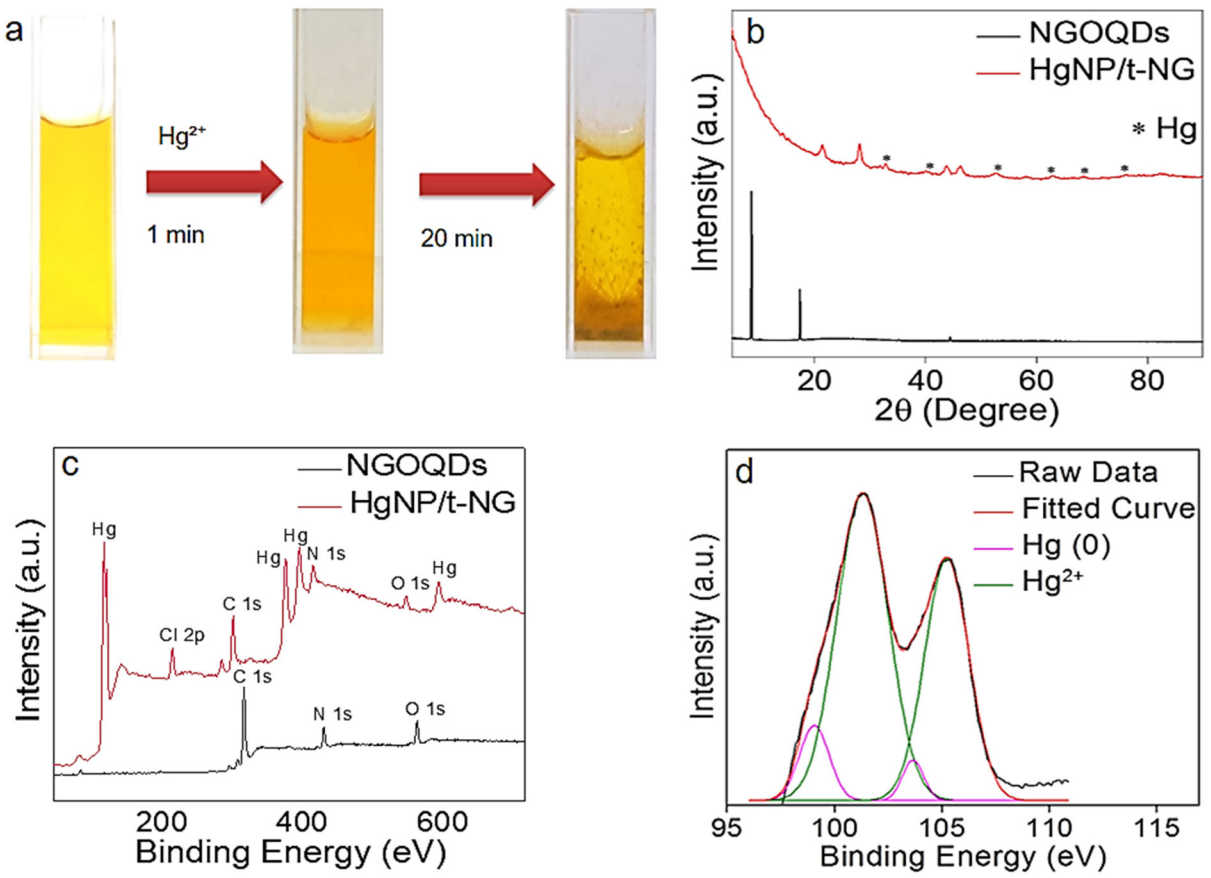


**Fig. 2** (a) Initial turbidity and precipitate formation after the addition of $Hg^{2+}$ to NGOQDs. Comparison of the (b) XRD pattern and (c) the XPS survey spectrum of NGOQDs and the HgNPs/t-NG matrix. (d) Deconvoluted Hg 4f XPS spectra of HgNPs on the t-NG matrix.

carbon framework from graphene oxide to reduced graphenic form is thus evident. The peak at $2\theta \sim 22°$ is characteristic of graphene layers with turbostratic disorder.[49] The interlayer spacing here is far larger (0.411 nm) than that of the Bernal stacking (0.334 nm) and indicates rotationally misoriented layers or increased interlayer distance.[50] Along with this, the peak at around 43° also justifies the turbostratic array of graphenic layers.[51] In addition, the peak near ~28° is also indicative of misaligned or disoriented graphene layers.[52] Excluding the other peaks corresponding to the carbon host matrix (peaks at $2\theta$ values of 22, 28, 43.1, and 46.4°), new peaks are observed in the XRD pattern at 32.8, 40.3, 52.7, 63.1, 68.3, and 76.2°. These are identified as peaks that originate from the rhombohedral α form of solid mercury with the corresponding (101), (003), (110), (104), (113) and (015) planes, and are in agreement with previous reports.[13,18,19] The result proves the formation of solid crystalline mercury, as bulk liquid mercury does not give an XRD pattern. In the XPS spectra (Fig. 2c and d), along with the usual peaks of the carbon core, oxygen and nitrogen, additional peaks are observed in the system, arising from mercury species. Peaks originating from Hg (0) are noted at 359, 378 and 577 eV, signifying Hg ($4d_{5/2}$), Hg ($4d_{3/2}$) and Hg ($4p_{3/2}$) states. The one centred at ~100 eV upon further splitting yielded peaks at 99 and 103.6 eV corresponding to the Hg (0) state (Fig. 2d) assigned, respectively to Hg ($4f_{7/2}$) and Hg ($4f_{5/2}$).[53] The additional pair of peaks found at 101.3 and 105.2 eV are indicative of the presence of excess $Hg^{2+}$ species in the adsorbed state. The peak corresponding to chlorine supports this argument.

TEM images of the solid material separated (Fig. 3a and b) show a drastic change in morphology when compared to the precursor NGOQDs, revealing sheet like structures. Extended sheet lattice, intercalating darker shades corresponding to metal species, is quite evident from the images, indicating that the NGOQDs have been subjected to metal ion induced face to face as well as edge to edge aggregation, in the presence of $Hg^{2+}$. The observation matches well with the studies conducted by Suter and coworkers, who have explored the metal ion induced aggregation of GO and GOQDs, and confirmed the decisive role of pH of the solution and C : O ratio in the carbon matrix in finalizing the morphology of the aggregates.[29] The distance between the graphene oxide flakes is highly decisive in the interaction of metal atoms with the former. At an interlayer distance of 0.8 nm $\leq d <$ 1.8 nm, the metal ion species is an "intercalated" environment.[29]

The dark regions signifying metal dispersion, appearing to be in continuous pattern, show distinct lattice fringes corresponding to atomic arrangements in solids in the high-resolution image (Fig. 3c), with a separation of 0.27 nm (Fig. S4(a), ESI†), agreeing with that of solid crystalline mercury.[18] Misaligned graphenic layers, characteristic of the turbostratic structural form,[54] are evident in Fig. 3d. Furthermore, from a zoomed version (Fig. 3e), the discontinuity in the carbon matrix is evident, that arises due to N-doping in the graphenic matrix, as is well established.[55,56] The $d$-spacing value calculated from the SAED pattern (Fig. 3f) matches that of the (110) plane of the solid rhombohedral α mercury phase, and is in agreement with the XRD analysis results. The results thus confirm the formation of 2D crystalline mercury intercalated in the t-NG matrix. The reductant role of NGOQDs makes them potential candidates for metal nanoparticle synthesis from salt precursors, paving the way to the abovementioned result.[43,57–59] Participation of oxygen functional groups anchored on a carbon framework in the said reduction process eventually leads to a decrease in the interplanar distance of carbon layers. Obviously this substantiates the absence of XRD peaks at lower $2\theta$ values corresponding the graphene oxide nature, and clearly indicates the conversion of the carbon matrix to reduced graphene oxide (rGO). A comparison of FT-IR spectra of the NGOQDs and the HgNP/t-NG system is provided in (Fig. 4a). A close similarity is observed in the spectral pattern, except for the reduction in the intensities of bands corresponding to functional groups, especially oxygen-containing groups.[18] Commendable reduction of the intensity of carboxylate and hydroxyl functionalities is striking here. The normalised FT-IR spectra show that no additional peak originated in the HgNP/t-NG system when compared to NGOQDs (Fig. S4 (b), ESI†). The Raman spectrum provides additional information regarding the defect structure of graphitic systems (Fig. 4b). The D and G bands were noted at 1367 and 1516 $cm^{-1}$, and the ratio of intensities of the peaks, an $I_D/I_G$ value of 0.80 noted for NGOQDs changed to 1.4 in the HgNP/t-NG composite and this can be justified by the increased number of defect states in porous graphene sheets, compared to the former. The Raman spectral data provide strong support for nanoparticle dispersion on graphene layers, from the strain induced in the layers. Apart from the Raman peaks seen in NGOQDs, a new band is generated by G band splitting, the D′ band, located at 1563.7 $cm^{-1}$, ascribed to bending strains resulting from the curvature of the carbon framework.[60] It is established that metal nanoparticle dispersion over the graphene sheet, eventually leads to strain induced sheet wrinkling.[61,62] Besides, the spectrum was distinct due to the presence of a discernible wide 2D band, positioned at ~2700 $cm^{-1}$, which confirms the few layer graphenic system. Usually, it is accepted that the 2D band (G′ band) can be fitted with a single Lorentzian peak with a larger full width at half maximum (FWHM) value for the turbostatic systems.[63] However, it is quite obvious that, though less intense, the above-mentioned peak originates from multiple peak components here, which can be justified by the dispersed metal nanoparticles. Folded few layer graphene is implied by this observation.[64] The 2D band broadening under strain, paving the way to multiple peaks in the 2D region is reported. Both experimental and theoretical proof was gained for this observation.[65] The broad band near 2200–3200 $cm^{-1}$, which can be split into components, explains a non-planar structure of graphene layers, and is generally found in metal nanoparticles entrapped in graphene.[66] A curve fitted second order Raman region presented in figure (Fig. S5, ESI†) shows four constituent bands upon curve fitting using Gaussian, positioned at 2485, 2734, 2883 and 3050 $cm^{-1}$, designated as G*, 2D, D + G

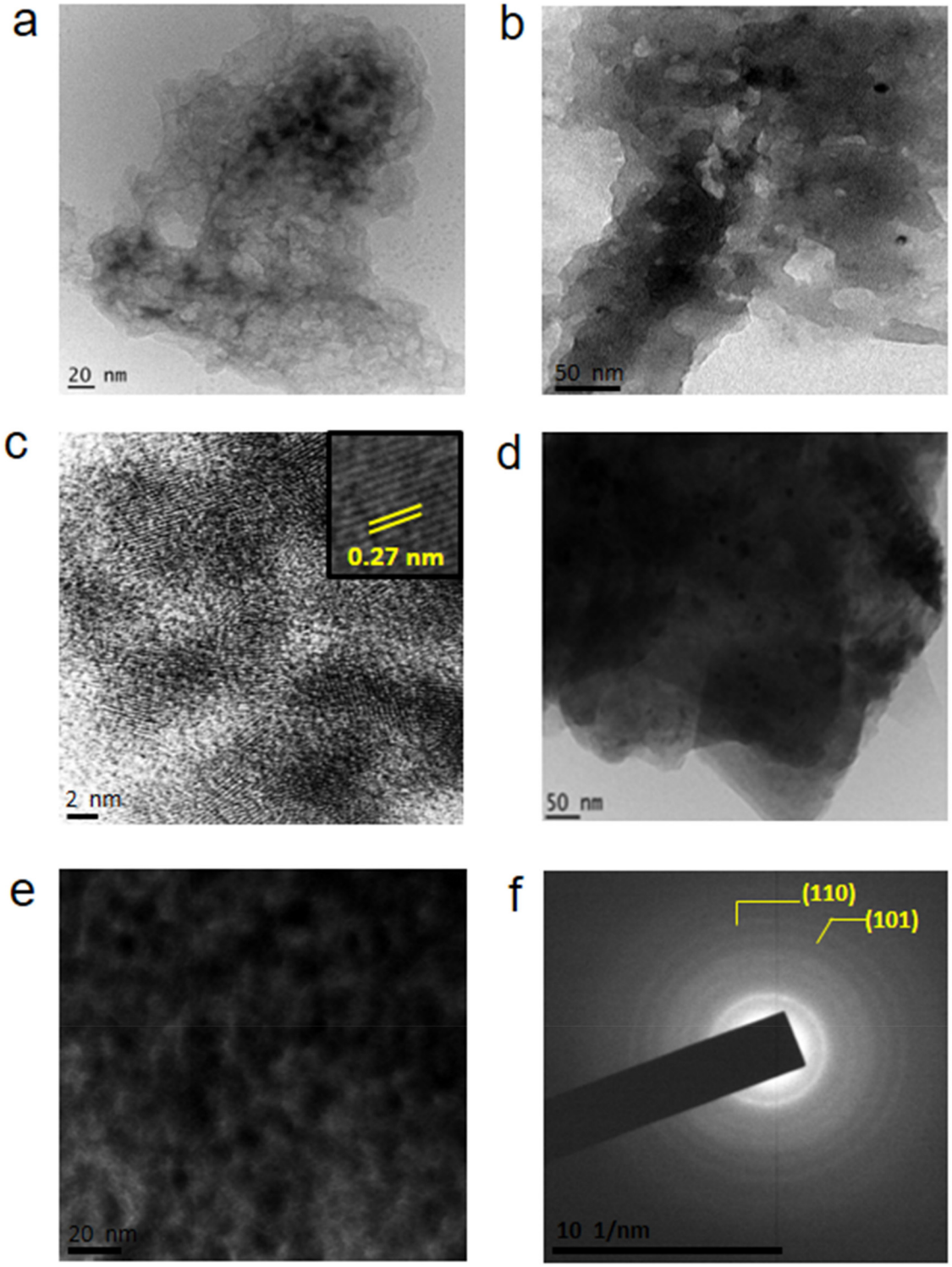


**Fig. 3** (a) Formation of graphene sheets. (b) Formation of solid mercury intercalated in graphene sheets. (c) Lattice fringes of solid state mercury, indicating a continuous lattice; inset shows a closer view of lattice fringes. (d) TEM image of the extended sheet structure, showing misaligned few-layered graphene. (e) Closer view of discontinuity in the N-doped graphenic matrix. (f) SAED pattern of the HgNP/t-NG system.

and $2D_2$ modes.[67] Evolution of D + G (3000 $cm^{-1}$) and $2D_2$ bands is attributed to the strained state of the graphene layer that is wrapped around metal nanoparticles.[66] Hence, a situation where the HgNPs are clad in randomly arranged graphene layers can be visualised in the HgNP/t-NG system. The low intensity bands noted at 1650–2250 $cm^{-1}$, the combination Raman bands, are characteristic of the turbostatic layer structure.[50,68–70] A shift in Raman spectral data of graphene is

 

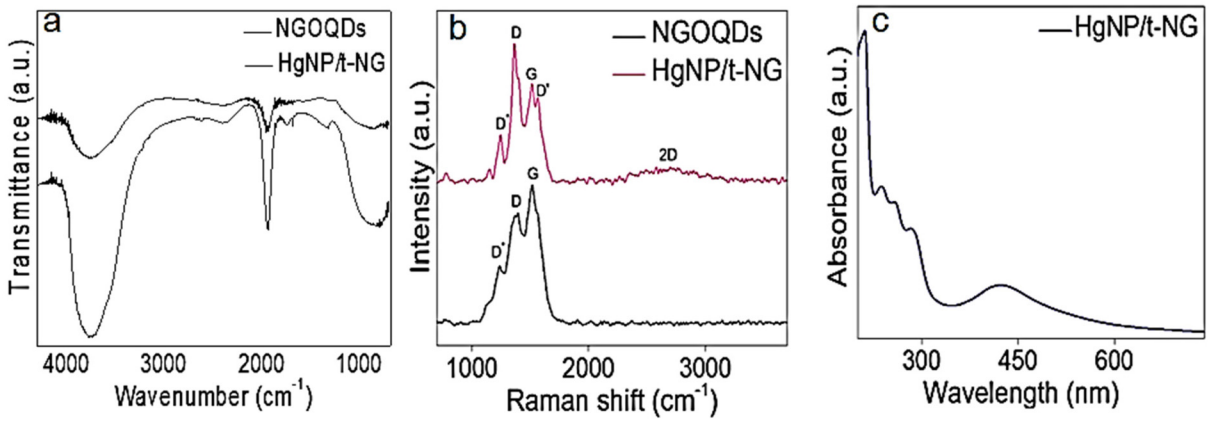


**Fig. 4** Comparison of FT-IR spectra (a) and Raman spectra (b) of NGOQDs and HgNPs on the t-NG matrix. (c) UV-vis absorption spectrum of the HgNP/t-NG system.



also noted, which is often associated with metal nanoparticle dispersion on sheets.[71] Thus Raman spectral data concludes HgNPs clad in graphenic layers in the system. Fig. 4c displays the UV-vis absorption spectrum of the HgNP/t-NG system. The spectrum is characterised by an absorption peak at ~280 nm, that matches well with that of nanoscale mercury, and is in agreement with previous reports.[12,18] The reduction of the GO form and partial restoration of π conjugation in the carbon matrix is established by the absorption peak at 260 nm, which is characteristic of graphenic systems.[72,73] The absorption peak at 420 nm justifies the n–π* transition in the carbon framework. Electron dispersive X-ray (EDX) analysis of the solid sample shows peaks corresponding to Hg, in addition to C, N and O elements present in nitrogen doped graphene (Fig. S4 (c), ESI†).

### 2.3. Formation of HgNP/t-NG matrix

TEM images have confirmed extended few layer graphenic matrix formation upon $Hg^{2+}$ addition to NGOQDs. pH and degree of oxidation are found to be decisive in controlling the final morphologies of metal ion induced aggregation of GO and GOQDs. pH dependent colloidal aggregation of GOQDs to expanded lattices in the presence of divalent metal ions is explored in detail by researchers.[27,28] Tang *et al.* used molecular dynamics simulations and density functional theory calculations to unveil the pH dependent aggregation mechanism of small GO flakes.[28] The study using different metal ions of variable valencies has shown that the GO flakes aggregate in the edge-to-edge mode independent of the ionic strength and nature and valency of cations in the pH range of 5–9. At pH > 6, the deprotonated carboxyl groups located on the peripheral carbons are engaged in interactions with metal ions,[28] leading to an edge to edge assembly, and directs lattice expansion in the plane leading to sheet morphology, as realized here at a pH value 7. It is established that the carboxyl groups are located at the edge carbon atoms in the graphenic layer. The drastic reduction in the intensity of carboxylate groups (that are established to be anchored on the edge carbons), as shown by the FT-IR spectrum after mercury ion incorporation justifies this assumption. However, the stacked layers observed in the TEM image (Fig. 3d) indicate the presence of face to face aggregation also, which can be substantiated by the lower oxygen content in the graphene matrix, as reported by Suter and co-workers.[29] Apart from pH, the extent of oxidation of GO/GOQD flakes plays a role in the final morphology of the matrix in the case of metal ion induced aggregations in aqueous solutions, as indicated by the molecular simulation studies conducted by them.[29] Lower oxidation functionalities (high C: O ratio) always favoured face–face aggregation in a stacked arrangement (H-type aggregation). More than 90% exists in the face to face aggregation for a C : O ratio >5 for divalent ions. A C : O ratio of ~10 can be assumed in the present case, neglecting the minor percentage of nitrogens present in the framework, as evident from the XPS data. The divalent ions remain bound to the nearest carboxylate ion, forming bridges between the carboxylate groups on different flakes and effectively reducing the repulsion between sheets, and also facilitating the face–face mechanism. This results in partial overlapping of flakes and edge–edge interactions *via* cation bridging.[29] While the face–face interactions require the flakes to remain approximately planar, the edge–edge interactions do not, in the end, resulting in a more open 3D structure with planar face–face aggregates joined together by cation bridging, which matches well with the observation collected from the TEM image (Fig. 3d). The charged end groups in the assembly at higher pH values cause misaligned flakes due to sheared alignment, so as to orient the former in sufficiently larger distances. The disoriented flakes prevent further layer stacking, preserving the few layer lattice structure. The same observation is valid here from the presence of turbostratic graphenic planes. The metal atoms are confirmed to be in the intercalated form when the GO flakes are 0.8 nm $\leq d <$ 1.8 nm,[29] and this adds strength to the argument of metal ion induced face to face aggregation of GO flakes. Subsequent to hydroxyl species mediated reduction, Hg(II) to Hg(0) conversion is realized. The reducing role of carbon nanodots and graphene quantum dots

is well documented in the literature, where they play a role in metal nanoparticle synthesis from corresponding metal ion precursors.[43,57,58]

The situation thus indicates the formation of mercury in the solid state in interlayers of graphene. The existence of mercury nanoparticles in the solid form requires high pressure or low temperature (1.2 GPa pressure/−38.83 °C temperature) as already mentioned, which is not provided under the present experimental conditions. The generation of van der Waals pressure on species trapped in interlayers of 2D materials comes into the scenario here. In order to further substantiate this, the AFM image of the system is used, as adopted by the previous researchers.[1] The AFM image (Fig. 5a) is indicative of arrays of misaligned graphene nanoflakes. This observation is in agreement with TEM data (Fig. 3d). A zoomed version shows the layer structure and the height profile along the marked line, which show sharp changes in the layer heights as the tip scans the rotationally misaligned layers in the turbostratic graphene matrix. The distance between individual nanoflakes was found to be normal ≤1 nm (Fig. 5b). This is further supported by XRD analysis which showed an interlayer distance of 0.71 nm in the HgNP/t-NG system. The metal atoms are confirmed to be in the intercalated form when the GO flakes are 0.8 nm ≤ $d$ < 1.8 nm in the initial state.[29] The entrapment of metal nanoparticles in the graphenic matrix is already confirmed the present case. The decrease in oxygen functionalities upon reduction further brings the interplanar distance down, as observed in the HgNP/t-NG system, which further adds pressure to the intercalated species in the interlayer space.[74] van der Waal pressure build up on molecules trapped between graphene layers is discussed in detail by the researchers, as already mentioned.[1,2,30] This pressure developed in such layer lattices is expected to generate two-dimensional crystals of the materials trapped in interlayers.[1] It was estimated that molecules confined in the interlayers of graphene of ~1 nm distance is subjected to 1.2 ± 0.3 GPa pressure, which is sufficient to modify the properties of a trapped material, and can even force the crystallization of a liquid well above its normal freezing temperature, which is realized in the present case. Thus, the criterion of ultra-high pressure requirement for mercury solidification is met, stabilizing the metal in solid form, and is well supported by precedented works.[1,2] The formation of the system is illustrated in Scheme 1.

The t-NG matrix effectively prevents the coalescence of individual ones to bulk liquid form. Previous work exploring the stability of HgNPs on rGO using theoretical modelling has confirmed that there exist electronic interactions with a slight charge transfer between the mercury that acts as the donor and the oxygen functionalities of rGO (acceptor), leading to the stabilization of the HgNPs on rGO, and enabling them to remain solid even at 150 °C temperature.[18] They have also shown that this stabilisation existed irrespective of the size of HgNPs. Such a charge transfer from the Hg atoms in the particles to the oxygen functionalities of graphene moieties creates ionic interactions between the Hg particles and the graphene sheets, together with van der Waals interactions. Analysis of the effect of the oxygen-containing groups on the graphene sheets show that this partial charge transfer is favored more on rGO compared to the unsubstituted graphene sheet. Enhanced stabilization of HgNPs with an increase in

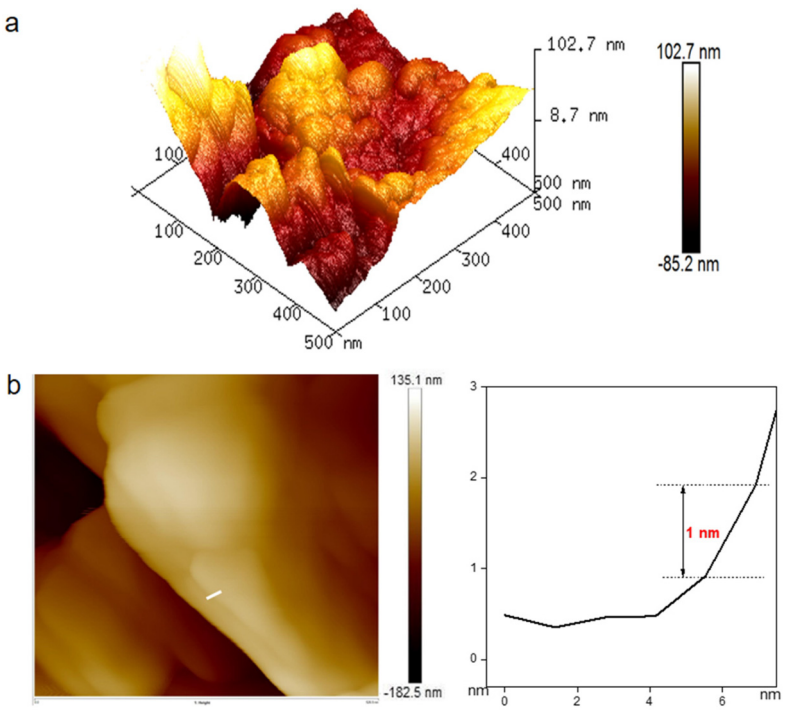


Fig. 5 (a) Graphene misaligned nanoflakes. (b) Zoomed version of the image to show the interlayer distance with the concerned plot.

 

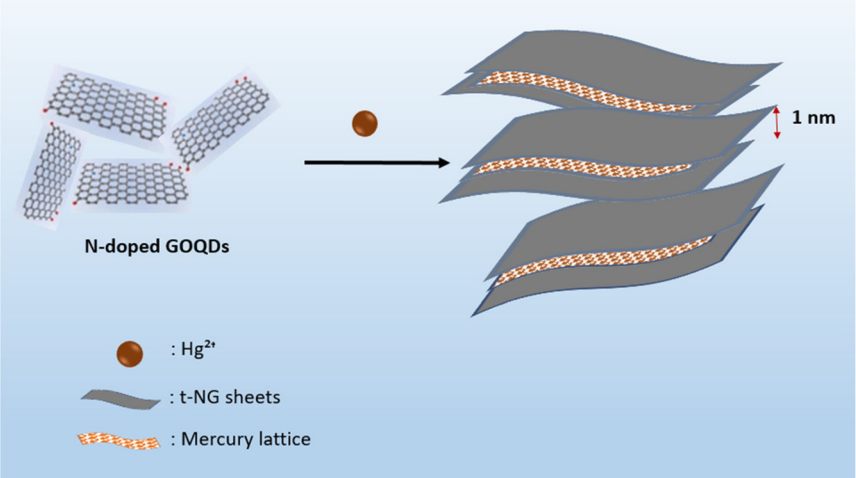


**Scheme 1** Illustration of HgNP/t-NG formation.

oxygen functionalities was also proved by them, as the interaction of metal particles with the carbon framework occurs through oxygen functional groups of the latter. The involvement of hydroxyl groups and epoxy groups was apparent.[18] The reduction in FTIR spectral bands at ~3500 $cm^{-1}$ and 1032 $cm^{-1}$ in the HgNP/t-NG system supports this proposal. Apart from the oxygen functional groups, the heteroatom nitrogen also contributes to the stable dispersal of the metal nanoparticles over the carbon framework. It is observed that framework nitrogen in the form of the pyridinic group overpower the oxygen functionalities in the system in providing the abovementioned stabilization sites.[24] Pyrrolic groups also act as good anchoring sites for the deposition of metal nanoparticles.[75,76] The pyridinic and pyrrolic groups observed in t-NG further validate the superior stability of HgNPs in the present scenario. This is confirmed by the involvement of nitrogen containing moieties, as evident from the curve fitted N 1s XPS data (Fig. S6, ESI†), indicated by the shift in binding energies[24] of pyridinic and pyrrolic groups (397.5 and 399 eV respectively), when compared to the parent NGOQDs. In addition, as already mentioned, the less compressible host matrix of exceptional mechanical strength in its turbostratic alignment favors the stability of the formed nanoparticles, by effective trapping of the HgNPs in the interlayer space.[19] The turbostratic structure of the matrix with misoriented sheets does play a role in dispersing the HgNPs over the matrix with appropriate steadiness, thus preventing the coalescence of the particles in the bulk liquid form. The stability of the solid state mercury achieved over time is confirmed from the stable XRD pattern corresponding to the material, collected after 6 months (Fig. S7, ESI†). Peaks corresponding to solid state mercury are retained, supporting the excellent stability of the sample.

### 2.4. A sustainable approach for toxic mercury ion detection and removal from wastewater

No introduction is needed on the toxicity of mercury(II), a highly soluble priority pollutant that poses extensive harm to human health and the environment. The conventional method followed for the abatement of mercury ions from the aqueous environment is adsorption using suitable adsorbents. Reverse osmosis using membranes is also practised. However, the management of the adsorbent/membrane after the analyte ion adsorption is another issue that is to be addressed. The present method of solid mercury formation on the t-NG matrix offers an effortless strategy for the detection, removal and safe storage of this toxic species using NGOQDs. Mere addition of NGOQDs to mercury ion containing aqueous solution realizes the separation of solid mercury entrapped in the t-NG structure within minutes (Fig. 2a). The results of the method using various other mercury precursors are shown in Fig. S8, ESI.† Solid separation after mercury salt addition is clearly visible. The solid mass separated can be easily filtered of using an ordinary filter paper after centrifugation, enabling the removal and safe disposal of the contaminant from the aqueous medium. As long as trapped in the graphenic matrix, the system retains the stable solid state, as illustrated by the XRD pattern collected after six months. To the best of our knowledge, this constitutes the most simple, efficient and green attempt at addressing mercury contamination in aqueous media. Fig. S9a, ESI† shows that the system is potent to perform excellently in real water samples (Fig. S9b, ESI†).

## 3. Conclusion

In this report, the synthesis of crystalline nanomercury confined in interlayers of nitrogen doped turbostratic graphenic matrix is presented. The reduction capability of NGOQDs, making them strong contenders for metal nanoparticle synthesis, is the key underpinning factor behind this finding. Concomitant involvement of pH and surface functional groups lead to the fabrication of misaligned graphene nanoflakes from NGOQDs, which restricts the metal in the solid state through nanoconfinement. $Hg^{2+}$ induced aggregation of

NGOQDs, directed by the solution pH and functional groups, weaves up the t-NG matrix, which evolves in a turbostratic fashion. Excellent stability of the material lasting for months warrants the scope of the system for further fine applications. The scope of layered 2D lattices in this direction is unveiled through this work. Furthermore, the strategy can be used for the detection, removal, and safe storage of mercury ions from contaminated aqueous solutions.

## Data availability

Data connected to this manuscript will be made available on request from the authors.

## Conflicts of interest

There are no conflicts to declare.

## Acknowledgements

A. T. P. acknowledges CSIR-UGC for the research fellowship. The authors are grateful to CIF-University of Calicut, for the analytical support. V. K. P. is grateful to the Council of Scientific and Industrial Research (CSIR) for providing the infrastructure and research facilities. R. N. K. gratefully acknowledges DST, Government of India, for the research facilities provided under FIST.



## References

1 K. Vasu, E. Prestat, J. Abraham, J. Dix, R. J. Kashtiban, J. Beheshtian, J. Sloan, P. Carbone, M. Neek-Amal and S. Haigh, *Nat. Commun.*, 2016, **7**, 12168.
2 G. Algara-Siller, O. Lehtinen, F. Wang, R. R. Nair, U. Kaiser, H. Wu, A. K. Geim and I. V. Grigorieva, *Nature*, 2015, **519**, 443–445.
3 C. H. Y. Xuan Lim, A. Sorkin, Q. Bao, A. Li, K. Zhang, M. Nesladek and K. P. Loh, *Nat. Commun.*, 2013, **4**, 1556.
4 K. Xu, P. Cao and J. R. Heath, *Science*, 2010, **329**, 1188–1191.
5 J. D. Blum, *Nat. Chem.*, 2013, **5**, 1066–1066.
6 G. Shafeev, F. Bozon-Verduraz and M. Robert, *Phys. Wave Phenom.*, 2007, **15**, 131–136.
7 L. Katsikas, M. Gutiérrez and A. Henglein, *J. Phys. Chem.*, 1996, **100**, 11203–11206.
8 A. Henglein and C. Brancewicz, *Chem. Mater.*, 1997, **9**, 2164–2167.
9 J. A. Creighton and D. G. Eadon, *J. Chem. Soc., Faraday Trans.*, 1991, **87**, 3881–3891.
10 S. Majumder, M. Priyadarshini, U. Subudhi, G. Chainy and S. Varma, *Appl. Surf. Sci.*, 2009, **256**, 438–442.
11 S. Majumder, M. Priyadarshini, U. Subudhi, M. Umananda, G. Chainy, P. Satyam and S. Varma, *Appl. Phys. Lett.*, 2009, **94**, 073110.
12 G. Ramesh, M. D. Prasad and T. Radhakrishnan, *Chem. Mater.*, 2011, **23**, 5231–5236.
13 A. Gedanken, E. Luvchik, J. Calderon-Moreno, N. Veglio and J. Tamarit, *Adv. Mater.*, 2008, **20**, 1000–1002.
14 K. Takemura, S. Nakano, Y. Ohishi, Y. Nakamoto and H. Fujihisa, *Mater. Res. Express*, 2014, **2**, 016502.
15 V. Kasperovich, E. Charnaya, C. Tien and C. Wur, *Phys. Solid State*, 2003, **45**, 1802–1807.
16 B. Borisov, E. Charnaya, P. Plotnikov, W.-D. Hoffmann, D. Michel, Y. A. Kumzerov, C. Tien and C.-S. Wur, *Phys. Rev. B:Condens. Matter Mater. Phys.*, 1998, **58**, 5329.
17 D. Michel, B. Borisov, E. Charnaya, W.-D. Hoffmann, P. Plotnikov and Y. A. Kumzerov, *Nanostruct. Mater.*, 1999, **12**, 515–518.
18 V. K. Harika, T. R. Penki, B. Loukya, A. Samanta, G.-L. Xu, C.-J. Sun, I. Grinberg, F. L. Deepak, K. Amine and D. Aurbach, *Chem. Sci.*, 2021, **12**, 3226–3238.
19 N. Kana, R. Morad, M. Akbari, M. Henini, J. Niemela, F. Hacque, A. Gibaud and M. Maaza, *Sci. Rep.*, 2022, **12**, 3494.
20 J. Donohue, *The Structures ofthe Elements*, John Wiley & Sons, New York, Sydney, Toronto, 1974.
21 K. Takemura, S. Nakano and Y. Ohisi, *Joint 20th AIRART-43th EHPRG. Karlsruhe*, *Germany*, 2005, pp. 342.
22 W. C. Lee, K. Kim, J. Park, J. Koo, H. Y. Jeong, H. Lee, D. A. Weitz, A. Zettl and S. Takeuchi, *Nat. Nanotechnol.*, 2015, **10**, 423–428.
23 Z. Wang, Y. Ping, Q. Fu and C. Pan, *MRS Adv.*, 2018, **3**, 849–854.
24 X. Xie, J. Long, J. Xu, L. Chen, Y. Wang, Z. Zhang and X. Wang, *RSC Adv.*, 2012, **2**, 12438–12446.
25 G. Goncalves, P. A. Marques, C. M. Granadeiro, H. I. Nogueira, M. Singh and J. Gracio, *Chem. Mater.*, 2009, **21**, 4796–4802.
26 I. Suarez-Martinez, C. Bittencourt, X. Ke, A. Felten, J. Pireaux, J. Ghijsen, W. Drube, G. Van Tendeloo and C. P. Ewels, *Carbon*, 2009, **47**, 1549–1554.
27 Q. Li, B. Chen and B. Xing, *Environ. Sci. Technol.*, 2017, **51**, 1364–1376.
28 H. Tang, S. Zhang, T. Huang, F. Cui and B. Xing, *Environ. Sci.:Nano*, 2020, **7**, 984–995.
29 J. L. Suter and P. V. Coveney, *Sci. Rep.*, 2021, **11**, 22460.
30 E. Khestanova, F. Guinea, L. Fumagalli, A. Geim and I. Grigorieva, *Nat. Commun.*, 2016, **7**, 12587.
31 B. Karimi and B. Ramezanzadeh, *J. Colloid Interface Sci.*, 2017, **493**, 62–76.
32 A. Shokry, M. Khalil, H. Ibrahim, M. Soliman and S. Ebrahim, *Sci. Rep.*, 2019, **9**, 16984.
33 Y. Zhu, Y. Zhu, H. Ni and R. Gu, *J. Phys.:Conf. Ser.*, 2023, **2539**, 012089.
34 R. Souza da Costa, W. Ferreira da Cunha, N. Simenremis Pereira and A. Marti Ceschin, *Materials*, 2018, **11**, 1492.
35 M. WooáLee and J. SangáSuh, *RSC Adv.*, 2015, **5**, 67669–67675.

 

36 P. Wu, W. Li, Q. Wu, Y. Liu and S. Liu, *RSC Adv.*, 2017, **7**, 44144–44153.
37 H. Miao, S. Li, Z. Wang, S. Sun, M. Kuang, Z. Liu and J. Yuan, *Int. J. Hydrogen Energy*, 2017, **42**, 28298–28308.
38 V. Dorogova, L. Yolshina, V. Pryakhina and E. Vovkotrub, *J. Inorg. Organomet. Polym. Mater.*, 2024, 1–20.
39 N. C. Martins, J. Ângelo, A. V. Girão, T. Trindade, L. Andrade and A. Mendes, *Appl. Catal., B*, 2016, **193**, 67–74.
40 B. Vinayan, N. I. Schwarzburger and M. Fichtner, *J. Mater. Chem. A*, 2015, **3**, 6810–6818.
41 M. Vedamalai, A. P. Periasamy, C.-W. Wang, Y.-T. Tseng, L.-C. Ho, C.-C. Shih and H.-T. Chang, *Nanoscale*, 2014, **6**, 13119–13125.
42 F. T. Johra, J.-W. Lee and W.-G. Jung, *J. Ind. Eng. Chem.*, 2014, **20**, 2883–2887.
43 P. V. Raveendran and N. Renuka, *Environ. Nanotechnol., Monit. Manage.*, 2022, **18**, 100676.
44 A. Y. Lee, K. Yang, N. D. Anh, C. Park, S. M. Lee, T. G. Lee and M. S. Jeong, *Appl. Surf. Sci.*, 2021, **536**, 147990.
45 Y. Feng, J. Zhao, X. Yan, F. Tang and Q. Xue, *Carbon*, 2014, **66**, 334–339.
46 S. Kang, K. M. Kim, K. Jung, Y. Son, S. Mhin, J. H. Ryu, K. B. Shim, B. Lee, H. Han and T. Song, *Sci. Rep.*, 2019, **9**, 4101.
47 Z.-H. Wen and X.-B. Yin, *RSC Adv.*, 2016, **6**, 27829–27835.
48 P. Varatharajan, I. S. Banu, M. H. Mamat and N. Vasimalai, *Phys. B*, 2023, **654**, 414703.
49 Y. Bian, B. He and J. Li, *BioResources*, 2016, **11**, 6299–6308.
50 K. Bhorkar, N. Samartzis, M. Athanasiou, L. Sygellou, N. Boukos, V. Dracopoulos, T. Ioannides and S. N. Yannopoulos, *npj 2D Mater. Appl.*, 2022, **6**, 56.
51 N. Sazali, M. Deraman, R. Omar, M. Othman, M. Suleman, S. Shamsudin, N. Tajuddin, M. Hanappi, E. Hamdan, N. Nor and N. H. Basri, *AIP Conf. Proc.*, 2016, **1784**, 040009.
52 M. D. Hossain, Q. Zhang, T. Cheng, W. A. Goddard III and Z. Luo, *Carbon*, 2021, **183**, 940–947.
53 Y.-W. Wang, Q. Liu, L. Wang, S. Tang, H.-H. Yang and H. Song, *Microchim. Acta*, 2019, **186**, 1–8.
54 E. Cuadros-Lugo, M. Piñon-Espitia, H. A. Martinez-Rodríguez, D. Lardizabal-Gutierrez, I. Estrada-Guel, J. M. Herrera-Ramirez and C. Carreño-Gallardo, *Materials*, 2022, **15**, 2501.
55 Y. Zhang, J. Ge, L. Wang, D. Wang, F. Ding, X. Tao and W. Chen, *Sci. Rep.*, 2013, **3**, 2771.
56 S. K. Singh, V. M. Dhavale, R. Boukherroub, S. Kurungot and S. Szunerits, *Appl. Mater. Today*, 2017, **8**, 141–149.
57 T. Liu, J. X. Dong, S. G. Liu, N. Li, S. M. Lin, Y. Z. Fan, J. L. Lei, H. Q. Luo and N. B. Li, *J. Hazard. Mater.*, 2017, **322**, 430–436.
58 X. Wang, L. Cao, F. Lu, M. J. Meziani, H. Li, G. Qi, B. Zhou, B. A. Harruff, F. Kermarrec and Y.-P. Sun, *Chem. Commun.*, 2009, 3774–3776.
59 V. Ansi, P. Sreelakshmi, R. Poovathinthodiyil and N. Renuka, *Mater. Res. Bull.*, 2021, **139**, 111284.
60 L. Song, L. Ci, L. Sun, C. Jin, L. Liu, W. Ma, D. Liu, X. Zhao, S. Luo and Z. Zhang, *Adv. Mater.*, 2006, **18**, 1817–1821.
61 J. Vejpravova, B. Pacakova, J. Endres, A. Mantlikova, T. Verhagen, V. Vales, O. Frank and M. Kalbac, *Sci. Rep.*, 2015, **5**, 15061.
62 W. Wang, S. Liang, T. Yu, D. Li, Y. Li and X. Han, *J. Appl. Phys.*, 2011, **109**, 07C501.
63 R. Kar and N. Maiti, *J. Nanopart. Res.*, 2021, **23**, 1–10.
64 Y. Hao, Y. Wang, L. Wang, Z. Ni, Z. Wang, R. Wang, C. K. Koo, Z. Shen and J. T. Thong, *Small*, 2010, **6**, 195–200.
65 O. Frank, M. Mohr, J. Maultzsch, C. Thomsen, I. Riaz, R. Jalil, K. S. Novoselov, G. Tsoukleri, J. Parthenios and K. Papagelis, *ACS Nano*, 2011, **5**, 2231–2239.
66 J. Lee, S. Shin, S. Kang, S. Lee, J. Seo and T. Lee, *J. Nanomater.*, 2015, **2015**, 975043.
67 O.-A. Lazar, A. Marinoiu, M. Raceanu, A. Pantazi, G. Mihai, M. Varlam and M. Enachescu, *Energies*, 2020, **13**, 4307.
68 J. A. Garlow, L. K. Barrett, L. Wu, K. Kisslinger, Y. Zhu and J. F. Pulecio, *Sci. Rep.*, 2016, **6**, 19804.
69 R. Rao, R. Podila, R. Tsuchikawa, J. Katoch, D. Tishler, A. M. Rao and M. Ishigami, *ACS Nano*, 2011, **5**, 1594–1599.
70 C. Cong, T. Yu, R. Saito, G. F. Dresselhaus and M. S. Dresselhaus, *ACS Nano*, 2011, **5**, 1600–1605.
71 X. Zheng, W. Chen, G. Wang, Y. Yu, S. Qin, J. Fang, F. Wang and X.-A. Zhang, *AIP Adv.*, 2015, **5**, 057133.
72 K. Yokwana, B. Ntsendwana, E. N. Nxumalo and S. D. Mhlanga, *J. Mater. Res.*, 2023, **38**, 3239–3263.
73 S. S. Dwitya, Y.-H. Hsueh, S. S.-S. Wang and K.-S. Lin, *Mater. Chem. Phys.*, 2023, **295**, 127135.
74 Y. Sekimoto, R. Ohtani, M. Nakamura, M. Koinuma, L. F. Lindoy and S. Hayami, *Sci. Rep.*, 2017, **7**, 12159.
75 R. I. Jafri, N. Rajalakshmi and S. Ramaprabhu, *J. Mater. Chem.*, 2010, **20**, 7114–7117.
76 G. Wu, D. Li, C. Dai, D. Wang and N. Li, *Langmuir*, 2008, **24**, 3566–3575.